

Compressive Sensing Imaging of Non-Sparse 2D Scatterers by a Total-Variation Approach Within the Born Approximation

Giacomo Oliveri, *Senior Member, IEEE*, Nicola Anselmi, *Graduate Student Member, IEEE*, and Andrea Massa, *Member, IEEE*

Abstract—The problem of imaging two-dimensional “non-sparse” scatterers with piecewise-constant contrast is solved through an innovative total-variation compressive sensing (TV-CS) technique. Under Born approximation (BA), the time-harmonic two-dimensional inverse scattering problem is reformulated into an equivalent Augmented Lagrangian one according to the TV-CS formulation. The resulting unconstrained functional is then minimized by means of a deterministic *alternating direction* algorithm. Selected results from a numerical assessment are discussed to give the interested reader some insights on the accuracy, the flexibility, the robustness, and the efficiency of the TV-CS inversion scheme also in comparison with available implementations of state-of-the-art inversion methods still formulated within the BA.

Index Terms—Augmented Lagrangian method, Born approximation (BA), convex programming, inverse scattering, microwave imaging, remote sensing, total-variation compressive sampling.

I. INTRODUCTION AND RATIONALE

THE development of robust and accurate inversion algorithms is a popular research area because of its potential impact in a wide range of applications as subsurface prospecting [1]–[4], non-destructive testing [5]–[7], remote sensing [8]–[10], biomedical diagnosis [11]–[16], through-the-wall imaging [17], and, more in general, microwave and optical imaging [18]–[21]. Nevertheless, fitting the requirements of fast convergence (quasi real-time in some applicative fields), high spatial resolution, and reliability still represents a very challenging task because of the intrinsic theoretical and practical difficulties in addressing the associated inverse problems [16], [18], [22]. Towards this end, an interesting class of approaches is aimed at exploiting the available *a-priori* information to mitigate the ill-posedness [16], [22] of the mathematical problem at hand. Within such a framework, the regularization [23] through *sparsity* priors has recently emerged as a powerful and efficient strategy to deduce robust and fast imaging methods for linear inverse scattering problems

[24]–[27]. More specifically, the compressive sensing (CS) paradigm [28]–[31] has been adopted to handle sparsity-regularized two-dimensional time-harmonic linear inverse problems formulated within the *contrast-source* framework (e.g., under transverse-magnetic (TM) [26] or transverse-electric (TE) [32] illuminations, eventually comprising “minimum-norm” reformulations [33]) or exploiting Born approximation (BA) [27] and Rytov (RA) approximations [34] also in the optical regime [21]. An extension to deal with metallic scatterers has been investigated [35], as well.

Despite the success and the effectiveness of these techniques, also recognized throughout comparisons with state-of-the-art inversion methods [26], [27], their applicability is currently limited to those applicative fields where the unknowns (e.g., the contrast function [27], the equivalent currents [26], or the local-shape function [35]) on which the sparsity prior is enforced can be faithfully represented with uniform/single-resolution “pixel” bases [27], [26], [35] (i.e., the unknowns are “sparse” with respect to single-resolution pixel bases). As a consequence, they turn out to be effective up till now only when “sparse profiles” (i.e., targets represented by few, generally non-connected, uniform pixels) are at hand, while “large” scatterers (i.e., scatterers composed by more single-resolution uniform connected pixels, thus ‘non-sparse’ with respect to single-resolution pixel bases) cannot be accurately retrieved.

To overcome such a limitation, two possible line-of-reasoning can be followed. On the one hand, the exploitation of multi-resolution “pixel” bases or “non-pixel” basis functions still within the CS formulations, already developed in [26], [27], can be considered. However, the choice of suitable bases requires some *a-priori* information on the class of objects under investigation since it must guarantee that any target of interest can be exactly represented by only few non-zero basis coefficients [28], [29]. Therefore, such a guideline is not very trivial unless the class of the retrieved profiles, to which the scatterer under test belongs to, is not accurately known in advance.

An alternative strategy to deal with ‘non uniform-pixel sparse’ scatterers, while still keeping a uniform pixel discretization of the investigation domain, consists in formulating the inversion problem within the CS environment with an *indirect* sparsity prior [36]–[38]. Towards this end, let us consider that the *discrete gradient* of the contrast of large (i.e., objects composed by multiple connected uniform-size pixels) piecewise-constant objects turns out sparse (i.e., it is zero everywhere except at the pixel belonging to the target

Manuscript received January 07, 2014; revised May 26, 2014; accepted July 25, 2014. Date of publication July 30, 2014; date of current version October 02, 2014.

The authors are with the ELEDIA Research Center@DISI, University of Trento, Povo 38123 Trento—Italy (e-mail: giacomo.oliveri@disi.unin.it; nicola.anselmi@disi.unin.it; andrea.massa@ing.unin.it).

Color versions of one or more of the figures in this paper are available online at <http://ieeexplore.ieee.org>.

Digital Object Identifier 10.1109/TAP.2014.2344673

edges). This assumption models several applicative scenarios including delamination retrieval in composite materials [39], bubble identification in foams [40], and underground tunnel detection [41], [42]. Accordingly, a CS-based formulation can be applied also in this case by enforcing the sparsity prior on the *discrete gradient* of the unknowns rather than on the unknowns themselves. The arising method, usually indicated as total variation compressive sensing (TV-CS),¹ has recently been widely adopted in image restoration problems [36]–[38] also introducing several solution tools such as SOCP [46], “ ℓ_1 -Magic” [47], TwIST [48], and NESTA [49]. Unfortunately, most of these latter either have slow convergence rates, mainly when a large number of degrees-of-freedom [DoFs] is handled [46]–[48], or require restrictive assumptions on the observation matrix [49] that cannot be always guaranteed in the inversion problems at hand.

More recently, a new approach has been developed where the original TV-CS problem has been firstly recast to the minimization of an augmented Lagrangian functional then carried out through an “alternating direction” algorithm [36]–[38]. This choice has proven to be more numerically efficient and without restrictions (e.g., real or complex-valued) on the observation matrix as it happens in [26], [27]. This paper is then aimed at introducing an innovative method based on such a TV-CS approach to the solution of two-dimensional time-harmonic inverse scattering problems comprising scatterers with piecewise-constant contrast, but “non-sparse” in a single-resolution pixel basis. Towards this end and within the first-order BA [50], [27], the linearized contrast-field formulation of the inversion problem is reformulated in the TV-CS framework following the guidelines detailed in [36]–[38]. Moreover, the deterministic *alternating direction* algorithm [36]–[38] is successively applied to retrieve the unknown contrast profile by minimizing the associated Augmented Lagrangian functional. The main methodological contributions of this work rely on (i) the derivation of a CS-based inverse scattering strategy that, unlike similar state-of-the-art methods [21], [26], [27], [32]–[35], effectively handles objects whose sparsity is not only with respect to a single-resolution pixel basis (e.g., objects composed by multiple connected single-resolution pixels or “large” scatterers still within the BA); (ii) the introduction of a sparsity-regularized solver able to deal with complex-valued matrices and vectors, unlike many existing CS-based imaging strategies that require suitable re-formulations of the original problem in a real-valued one [33]; (iii) the generalization of TV-CS solution methods to electromagnetic imaging problems by suitably extending and customizing the original Augmented Lagrangian approach [36]–[38]; (iv) the application of a TV-regularized imaging scheme that, unlike existing TV-based inversion methods [45], comprises an ℓ_1 -norm TV term (rather than the usual ℓ_2 term [45]).

The outline of the paper is as follows. After the formulation of the first-order BA inverse scattering problem within the TV-CS framework (Section II), the proposed inversion method will be described in Section III. A selected set of numerical results will

be then illustrated to assess its effectiveness and limitations also throughout some comparisons with available implementations of state-of-the-art deterministic and CS strategies (Section IV). Finally, some conclusions are drawn (Section V).

II. PROBLEM STATEMENT

Let us consider a two-dimensional imaging problem where a set of “weak” scatterers [50] are located in an investigation domain D , which is successively illuminated by V known incident transverse-magnetic (TM_z) plane waves of amplitudes $F_v(\mathbf{r})$, $v = 1, \dots, V$. Let the scatterers be modeled by the contrast function

$$\tau(\mathbf{r}) \triangleq [\varepsilon_r(\mathbf{r}) - 1] - j \left[\frac{\sigma(\mathbf{r})}{2\pi f \varepsilon_0} \right] \quad (1)$$

$\mathbf{r} = (x, y)$ being the coordinate vector and where $\varepsilon_r(\mathbf{r})$ is the relative dielectric permittivity, $\sigma(\mathbf{r})$ is the conductivity, and ε_0 is the permittivity of the homogeneous lossless background. Within the first-order BA [50], the scattered electric field $E_v(\mathbf{r})$ [$E_v(\mathbf{r}) \triangleq T_v(\mathbf{r}) - F_v(\mathbf{r})$] in the observation domain C complies with the following *Data Equation*

$$E_v(\mathbf{r}) = \int_D \tau(\mathbf{r}') F_v(\mathbf{r}') G(\mathbf{r}/\mathbf{r}') d\mathbf{r}' \quad \mathbf{r} \in C, \mathbf{r} \notin D, v = 1, \dots, V \quad (2)$$

where $T_v(\mathbf{r})$ is the total electric field and $G(\mathbf{r}/\mathbf{r}')$ is the two-dimensional free-space Green’s function.

The retrieval procedure is then aimed at numerically inverting (2) starting from the knowledge of the incident field $F_v(\mathbf{r})$ and the samples of the scattered electric field, $E_v(\mathbf{r}_v^m)$, measured at M probing locations, $\mathbf{r}_v^m \in C$, $m = 0, \dots, M-1$. Towards this end, the unknown profile $\tau(\mathbf{r})$ is then modeled as a piecewise constant function through discretization. More specifically, the contrast function within D is discretized as follows

$$\tau(\mathbf{r}) = \sum_{p=1}^P \sum_{q=1}^Q \tau^{(p,q)} \varphi^{(p,q)}(\mathbf{r}) \quad (3)$$

where $\Phi = \{\varphi^{(p,q)}(\mathbf{r}), p = 0, \dots, P-1, q = 0, \dots, Q-1\}$ is the uniform single-resolution “pixel” basis (comprising $N \triangleq P \times Q$ pixels) whose (p, q) -th element is defined as

$$\varphi^{(p,q)}(\mathbf{r}) = \begin{cases} 1 & \mathbf{r} \in D^{(p,q)} \\ 0 & \mathbf{r} \notin D^{(p,q)} \end{cases} \quad p = 0, \dots, P-1, q = 0, \dots, Q-1 \quad (4)$$

$D^{(p,q)}$ being the spatial support of the (p, q) -th pixel ($\bigcup_{p=1}^P \bigcup_{q=1}^Q D^{(p,q)} = D$). By substituting (3) in (2) and after simple mathematical manipulations, the following matrix relation can be yielded

$$\mathbf{E}_v = \mathcal{G}_v \boldsymbol{\tau} \quad v = 0, \dots, V-1 \quad (5)$$

where $\mathbf{E}_v = \{E_v(\mathbf{r}_v^m); m = 0, \dots, M-1\}$, $\boldsymbol{\tau} = \{\tau^{(n)} \triangleq \tau^{(p,q)}; p = n \bmod P, q = \lfloor n/P \rfloor, n = 0, \dots, N-1\}$ is the (single-resolution piecewise-constant) vector of the unknowns, and $\mathcal{G}_v = \{g_v^{mn}; m = 0, \dots, M-1, n = 0, \dots, N-1\}$

¹The arising formulation differs from that of standard TV methods adopted in imaging [43]–[45] since it maximizes the *sparsity* of the discrete gradient, rather than minimizing its *energy* [45].

²For the sake of conciseness, the assumed time dependency factor $\exp(-j2\pi ft)$ is omitted hereinafter.

is the Green's matrix (also named *observation matrix*) whose (mn) -entry is given by $g_v^{mn} \triangleq \int_D \varphi^{(n)}(\mathbf{r}') F_v(\mathbf{r}') G(\mathbf{r}_v^m/\mathbf{r}') d\mathbf{r}'$ being $\varphi^{(n)}(\mathbf{r}') \triangleq \varphi^{(p,q)}(\mathbf{r}')$, $p = n \bmod P$, $q = \lfloor n/P \rfloor$, $n = 0, \dots, N-1$.

In retrieving τ from (5), the *piecewise-constant* nature of the targets can be profitably exploited as *a-priori* information to formulate the inverse problem at hand within the CS framework. Indeed, although single-resolution piecewise-constant contrasts are not always sparse, but only for single-pixel or multiple-pixels disconnected objects, the corresponding *gradient*

$$\nabla \tau = \{\nabla_x \tau, \nabla_y \tau\} \quad (6)$$

turns out to be *sparse* since its non-zero entries are only at the locations of the pixels in the object contour (i.e., the discontinuities of the contrast function within D). In (6), $\nabla \tau \in \mathbb{C}^{2N}$, $\nabla_x \tau = \{\nabla_x \tau^{(n)} \triangleq \nabla_x \tau^{(p,q)} = \tau^{(p,q)} - \tau^{(p-1,q)}; p = n \bmod P, q = \lfloor n/P \rfloor, n = 0, \dots, N-1\}$ and $\nabla_y \tau = \{\nabla_y \tau^{(n)} \triangleq \nabla_y \tau^{(p,q)} = \tau^{(p,q)} - \tau^{(p,q-1)}; p = n \bmod P, q = \lfloor n/P \rfloor, n = 0, \dots, N-1\}$ being the x and y components of the gradient, respectively.³ The information on the sparseness of $\nabla \tau$ is thus exploited by formulating the imaging problem in the following TV-CS fashion [36]–[38]

TV-CS Problem—Given $\mathbf{E}_v \in \mathbb{C}^M$, solve (5) by computing

$$\begin{aligned} \hat{\tau}_v &= \arg\{\min_{\tau} \|\nabla \tau\|_1\} \\ \text{s.t. } \mathcal{G}_v \tau &= \mathbf{E}_v \quad v = 0, \dots, V-1. \end{aligned} \quad (7)$$

In (7), $\|\cdot\|_1$ is the ℓ_1 -norm, while $\hat{\tau}_v$ is the TV-CS-based estimate of the contrast in correspondence with the v -th illumination. Finally, the retrieved contrast, $\hat{\tau}$, is computed by averaging the V estimates $\{\hat{\tau}_v; v = 1, \dots, V\}$:

$$\hat{\tau} = \frac{1}{V} \sum_{v=1}^V \hat{\tau}_v. \quad (8)$$

III. TOTAL VARIATION CS INVERSION

Because of the non-differentiability and the non-linearity of the TV term, $\|\nabla_x \tau\|_1 + \|\nabla_y \tau\|_1$, (7) cannot be easily solved⁴ and different strategies have been proposed in the state-of-the-art literature [46]–[48]. The second-order cone programming (SOCP) tool has been developed in [46] by exploiting the interior point method, but the arising solver turned out to be quite slow due to the need of solving a linear system at each iteration of the searching procedure [46], [36]. To overcome such a drawback, the ℓ_1 -Magic tool still considers the second-order cone formulation, but it resorts to a *log-barrier* search method [47]. Although more efficient than SOCP, the ℓ_1 -Magic solver becomes too time

³Such a formulation can be applied whatever the boundary condition to compute $\nabla \tau$ at the edge of D (e.g., the value of $\tau^{(p-1,q)}$ when $p = 0$, which is needed to compute $\nabla_x \tau^{(p,q)}|_{p=0}$) [36]. Without loss of generality, a periodic boundary condition will be considered hereinafter (i.e., $\tau^{(p-1,q)}|_{p=0} \triangleq \tau^{(p-1,q)}|_{p=P}$) [36].

⁴This problem feature is fundamentally different from what happens in standard TV approaches (which comprise ℓ_2 -norm terms) [45].

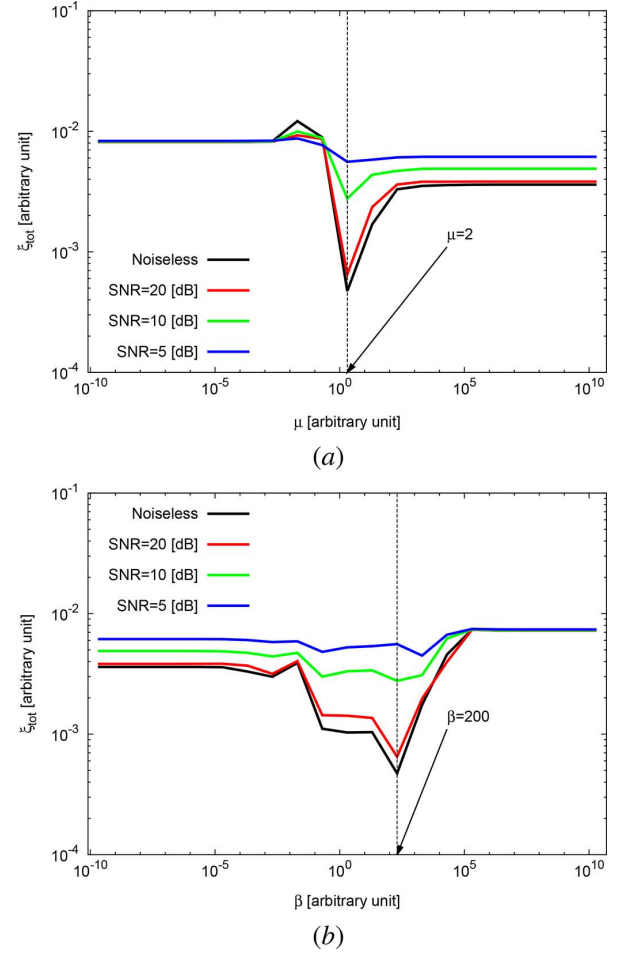


Fig. 1. Calibration (“Square” profile, $L = 2/3\lambda$, $\tau = 0.1$)—Behavior of ξ_{tot} versus (a) μ ($\beta = 200$) and (b) β ($\mu = 2.0$).

consuming when handling large problems [36]. More recently, iterative shrinkage-thresholding (IST) methods have been proposed (e.g., TwIST [48] and NESTA [49]). Unfortunately, most of these implementations either show a slow convergence rate after few iterations [48] or they require the observation matrix complies with very strict rules (e.g., $\mathcal{G}_v \mathcal{G}_v^*$ is an orthogonal projector [49], \cdot^* being the conjugate transpose operator).

In this work, a deterministic *alternating direction* method developed in [36]–[38] is adopted. Following the guidelines in [36], an equivalent *convex* minimization problem is dealt with instead of directly handling (7). More in detail, the *convex* minimization problem at hand is

$$\min_{\tau, \mathbf{w}} \|\mathbf{w}\|_1 \quad \text{s.t. } \nabla \tau = \mathbf{w} \text{ and } \mathcal{G}_v \tau = \mathbf{E}_v \quad v = 0, \dots, V-1 \quad (9)$$

where $\mathbf{w} = \{w^{(n)}, n = 0, \dots, 2N-1\}$ is the auxiliary variable used to convexify the problem [36]. According to the Lagrangian multiplier method [51], the solution of (9) is equivalent to that of the following one

$$\begin{aligned} \min_{\tau, \mathbf{w}, \boldsymbol{\nu}, \boldsymbol{\gamma}} \quad & \mathcal{L}_v(\tau, \mathbf{w}, \boldsymbol{\nu}, \boldsymbol{\gamma}) \\ \text{s.t. } \quad & \nabla \tau = \mathbf{w} \text{ and } \mathcal{G}_v \tau = \mathbf{E}_v \quad v = 0, \dots, V-1 \end{aligned} \quad (10)$$

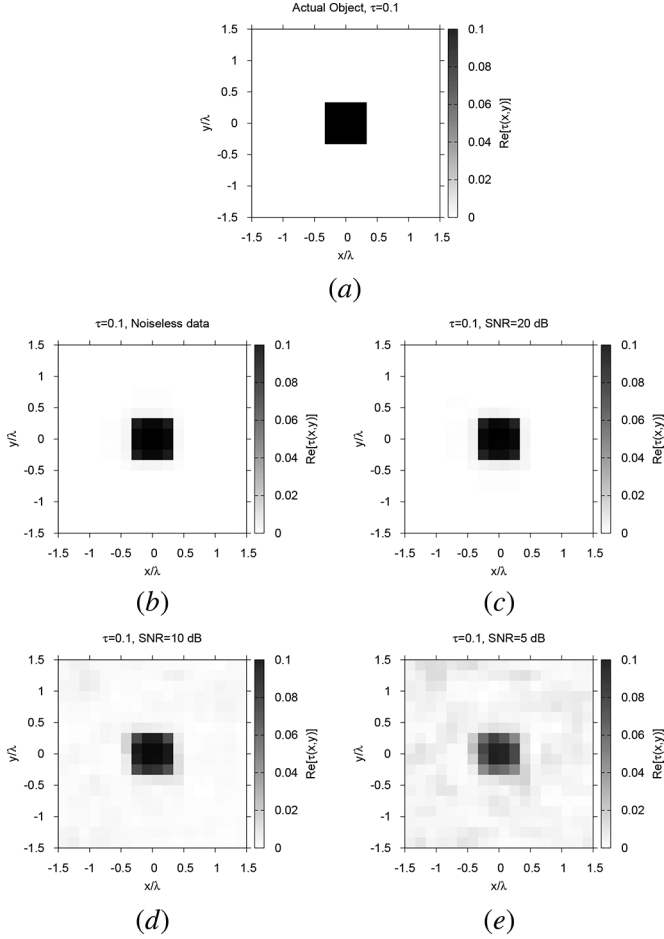


Fig. 2. Calibration (“Square” profile, $L = 2/3\lambda$, $\tau = 0.1$)—Actual (a) and retrieved (b)–(e) dielectric profiles when (b) SNR = ∞ , (c) SNR = 20 dB, (d) SNR = 10 dB, and (e) SNR = 5 dB.

where $\mathcal{L}_v(\tau, \mathbf{w}, \nu, \gamma) \triangleq |\mathbf{w}|_1 - \nu^*(\nabla\tau - \mathbf{w}) - \gamma^*(\mathcal{G}_v\tau - \mathbf{E}_v)$ is the Lagrangian function and $\nu \triangleq \{\nu^{(n)}, n = 0, 2N-1\}$ and $\gamma \triangleq \{\gamma_m, m = 0, M-1\}$ are the Lagrangian multiplier vectors [51]. Although convex, solving (10) is still a non-trivial task because of its constrained, non-linear, and non-differentiable nature [36]. Towards this end, the idea behind the *Augmented Lagrangian* approach is to reformulate (10) into an unconstrained problem by adding to $\mathcal{L}(\tau, \mathbf{w}, \nu, \gamma)$ suitable “penalty terms” to account for the constraint mismatch [36]. Mathematically, it means

$$\min_{\tau, \mathbf{w}, \nu, \gamma} [\mathcal{A}_v(\tau, \mathbf{w}, \nu, \gamma)] \quad v = 0, \dots, V-1 \quad (11)$$

where

$$\mathcal{A}_v(\tau, \mathbf{w}, \nu, \gamma) \triangleq |\mathbf{w}|_1 - \nu^*(\nabla\tau - \mathbf{w}) - \gamma^*(\mathcal{G}_v\tau - \mathbf{E}_v) + \frac{\beta}{2} \|\nabla\tau - \mathbf{w}\|_2^2 + \frac{\mu}{2} \|\mathcal{G}_v\tau - \mathbf{E}_v\|_2^2 \quad v = 0, \dots, V-1 \quad (12)$$

is the *Augmented Lagrange function*, $\|\cdot\|_2$ is the ℓ_2 -norm, and β and μ are two (user-defined) barrier parameters. Now, the arising Augmented Lagrangian problem (11) is convex and unconstrained, but the functional (12) is still non-differentiable because of the presence of the “ ∇ ” terms. To properly address such an issue, the iterative alternating direction algorithm [51],

[52] recently developed by Li [36] is applied. It consists of a nested iterative procedure comprising an outer loop (k being the outer-loop iteration index, $k = 0, \dots, K-1$) and an inner loop (i being the inner-loop iteration index, $i = 0, \dots, I-1$) and it is carried out to (independently) find each v -th estimate $\hat{\tau}_v$ ($v = 0, \dots, V-1$).

More in detail, the fundamental idea is to minimize (12) by alternatively solving two sub-problems, that is the “ \mathbf{w} sub-problem” [i.e., minimization of (12) with respect to \mathbf{w}] and the “ τ sub-problem” [i.e., minimization of (12) with respect to τ]. Indeed, it turns out that the \mathbf{w} sub-problem can be easily solved as it admits a unique and closed-form solution for each step of the alternating minimization [36]. On the other hand, since the τ sub-problem is quadratic, its solution could be found by an iterative steepest descent procedure [36]. However, this approach would turn out too computationally expensive, as it would be necessarily repeated at each step of the alternating minimization [36]. Accordingly, a more efficient strategy is adopted to solve the τ sub-problem which is based on a *single-step steepest descent* approach, in which the “aggressive” step length is computed following the Barzilai-Borwein formula [36]. Accordingly, the following phases are iteratively repeated for each v -th illumination:

- 1) **Outer loop (Outer Initialization)**—Set $k = 0$, $\gamma|_k = \mathbf{0}$, $\nu|_k = \mathbf{0}$, $\tau|_k \triangleq (\mathcal{G}_v^* \mathcal{G}_v) \mathcal{G}_v^* \mathbf{E}_v$, and [36]
- $$\mathbf{w}|_k = \left\{ w^{(n)}|_k = \max \left\{ \left| z^{(n)}|_k \right|, 0.0 \right\} \operatorname{sgn} \left(z^{(n)}|_k \right) \right. \\ \left. n = 0, \dots, 2N-1 \right\} \quad (13)$$

where $z^{(n)}|_k \triangleq [\nabla\tau]^{(n)}|_k - (\nu^{(n)}|_k/\beta)$ and $\operatorname{sgn}(\cdot)$ stands for the *sign* operator;

- 2) **Inner loop (Inner Initialization)**—Set $i = 0$, $\mathbf{w}|_k^i \triangleq \mathbf{w}|_k$, and $\tau|_k^i \triangleq \tau|_k$;
- 3) **Inner loop (Residual Evaluation)**—Compute $R|_k^i \triangleq \mathcal{A}_v(\tau|_k^i, \mathbf{w}|_k^i, \nu|_k, \gamma|_k)$ with (12);
- 4) **Inner loop (Auxiliary-Variable Update)**—Evaluate $\mathbf{w}|_k^{i+1}$ with (13) being $z^{(n)}|_k \leftarrow z^{(n)}|_k^i \triangleq [\nabla\tau]^{(n)}|_k^i - (\nu^{(n)}|_k^i/\beta)$ (solution of the “ \mathbf{w} sub-problem”);
- 5) **Inner loop (Aggressive Step-Length Computation)**—Evaluate $\alpha|_k^{i+1}$ according to the Barzilai-Borwein formula

$$\alpha|_k^{i+1} \triangleq \frac{(\tau|_k^{i+1} - \tau|_k^i)^* (\tau|_k^{i+1} - \tau|_k^i)}{(\tau|_k^{i+1} - \tau|_k^i)^* (\mathbf{d}|_k^{i+1} - \mathbf{d}|_k^i)}$$

where $\mathbf{d}|_k^i \triangleq \beta \nabla^* (\nabla\tau|_k^i - \mathbf{w}|_k^i) - \nabla^* \nu|_k + \mu \mathcal{G}_v^* (\mathcal{G}_v \tau|_k^i - \mathbf{E}_v) - \mathcal{G}_v^* \gamma|_k$ is the gradient of the Augmented Lagrangian function, ∇^* being the transpose of the discrete gradient operator (6);

- 6) **Inner loop (Step-Length Check)**—Update $\alpha|_k^{i+1} \leftarrow \rho \alpha|_k^{i+1}$ until the *non-monotone Armijo* condition given by

$$\mathcal{A}_v(\tau|_k^i - \alpha|_k^{i+1} \mathbf{d}|_k^i, \mathbf{w}|_k^i, \nu|_k, \gamma|_k) \leq R|_k^i - \eta \alpha|_k^{i+1} \mathbf{d}|_k^{i*} | \mathbf{d}|_k^i| \quad (14)$$

holds true;

- 7) **Inner loop (Contrast Update)**—Compute $\tau|_k^{i+1} = \tau|_k^i - \alpha|_k^{i+1} \mathbf{d}|_k^i$ (solution of the “ τ sub-problem”);

- 8) **Inner loop (Inner-Convergence Check)**—If $(|\tau|_k^{i+1} - \tau|_k^i|_2 / |\tau|_k^i|_2) \leq \delta_{\text{in}}$ then $\tau|_{k+1} \triangleq \tau|_k^{i+1}$ and goto *Step 9*. Otherwise, $i \leftarrow i + 1$ and goto *Step 3*;
- 9) **Outer loop (Multipliers Update)**—Compute $\gamma|_{k+1} = \gamma|_k - \beta(\nabla \tau|_{k+1} - \mathbf{w}|_k)$ and $\nu|_{k+1} = \nu|_k - \mu(\mathcal{G}_v \tau|_k - \mathbf{E}_v)$;
- 10) **Outer loop (Outer-Convergence Check)**—If $(|\tau|_{k+1} - \tau|_k|_2 / |\tau|_k|_2) \leq \delta_{\text{out}}$ then $\hat{\tau}_v = \tau|_{k+1}$ and return. Otherwise, $k \leftarrow k + 1$ and go to *Step 2*.

It is worth remarking that, unlike *Bayesian CS* techniques [27], [33], the deduced algorithm seamlessly handles complex quantities (i.e., \mathcal{G}_v , τ , and \mathbf{E}_v), thus avoiding the reformulation procedures usually applied in other state-of-the-art CS imaging strategies [27], [33].

IV. NUMERICAL ASSESSMENT

This section is devoted to (a) the evaluation of the sensitivity of the TV-CS method on its control parameters (Section IV-A) and (b) the assessment of its accuracy, robustness, and computational efficiency when dealing with various scatterer types and noisy conditions (Section IV-B) also in comparison with pertinent and available state-of-the-art imaging method implementations (Section IV-C).

As reference scenario, a $d = 3.0\lambda$ -sided square investigation domain, D , has been illuminated by a set of $V = 27$ plane TM waves with incidence angles $\theta_v = (2\pi v/V)$, $v = 0, \dots, V-1$ and it has been partitioned into $N_{FS} = 36 \times 36$ uniform square $(\lambda/12)$ -sided cells/pixels. The numerically-computed scattered field [53] has been then collected at $M = 27$ points located on a circular observation domain ($c = 3.0\lambda$ in radius) at $\mathbf{r}_v^m = [c \times \cos(2\pi m/M), c \times \sin(2\pi m/M)]$, $m = 0, \dots, M-1$. Starting from such scattered field data, the TV-CS inversion has been performed by discretizing D with a uniform grid of $N = P \times Q = 324$ ($P = Q$) equal sub-domains verifying the condition $N_{FS} \neq N$ to avoid the “inverse crime” [22], while guaranteeing a suitable spatial resolution of the reconstruction. In order to evaluate the inversion performance, the distribution of the actual/reconstructed contrast profiles will be reported, but the values of the following error indexes

$$\xi_O \triangleq \frac{1}{\text{Area}(D_O)} \int_{D_O} \frac{|\hat{\tau}(\mathbf{r}) - \tau(\mathbf{r})|}{|\tau(\mathbf{r}) + 1|} d\mathbf{r}, \quad O = \text{tot}, \text{int}, \text{ext} \quad (15)$$

will be also given for a more quantitative indication.

A. TV-CS Calibration

The first set of numerical experiments is aimed at evaluating the sensitivity of the TV-CS procedure on its control parameters as well as setting their ‘optimal’ trade-off values. According to the guidelines in [36], the control parameters δ_{out} , δ_{in} , η , and ρ have been set to their default values ($\delta_{\text{out}} = \delta_{\text{in}} = 10^{-3}$, $\eta = 10^{-5}$, $\rho = 0.6$) because of their marginal impact on the TV-CS performance as claimed in [36]. On the contrary, the choice of β and μ has been carefully addressed because of their expected and direct impact on the definition of the Augmented Lagrangian function (12) [36]. Towards this end and

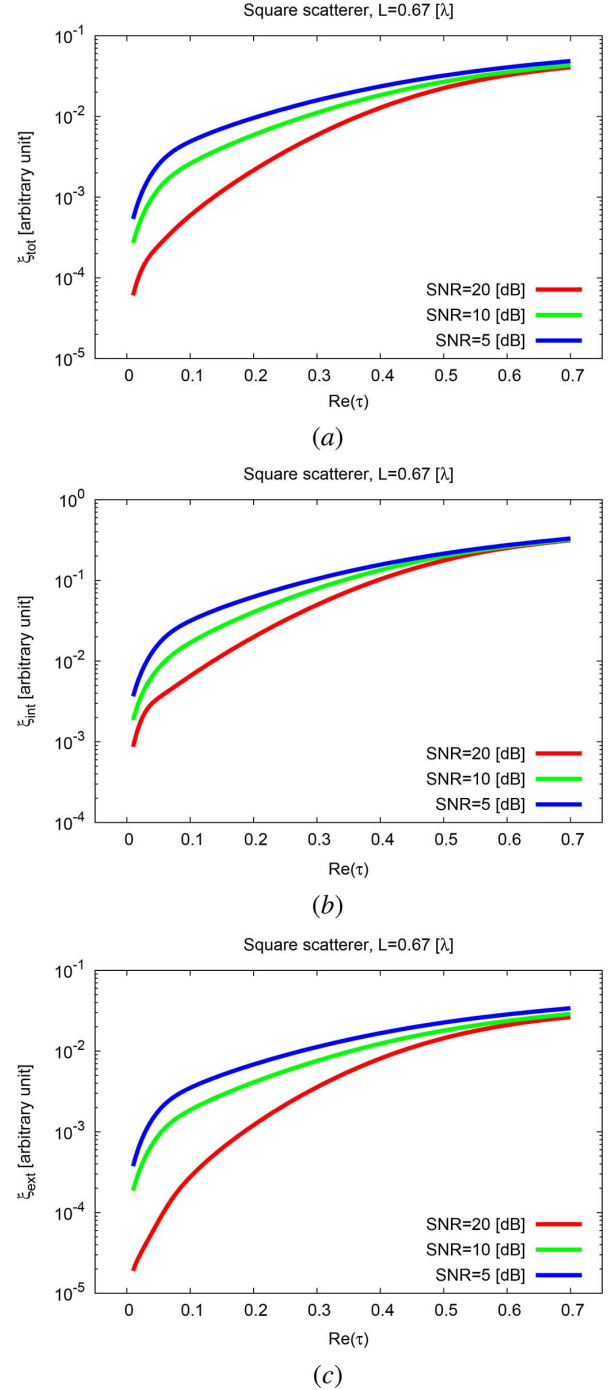


Fig. 3. Performance Assessment (“Square” profile, $L = 2/3\lambda$)—Behavior of (a) ξ_{tot} , (b) ξ_{int} , and (c) ξ_{ext} versus τ for different SNR values.

throughout the whole calibration process, a $\tau = 0.1$ square scatterer of side $L = 2/3\lambda$ [i.e., a set of 16 connected pixels within D —Fig. 2(a)] centered at the origin has been assumed as a benchmark imaging configuration. Moreover, several reconstructions have been carried out starting from various scattering data characterized by multiple realizations of different signal-to-noise ratios (SNRs).⁵

⁵In this work, the SNR is defined with respect to the scattered field as in [27], [33].

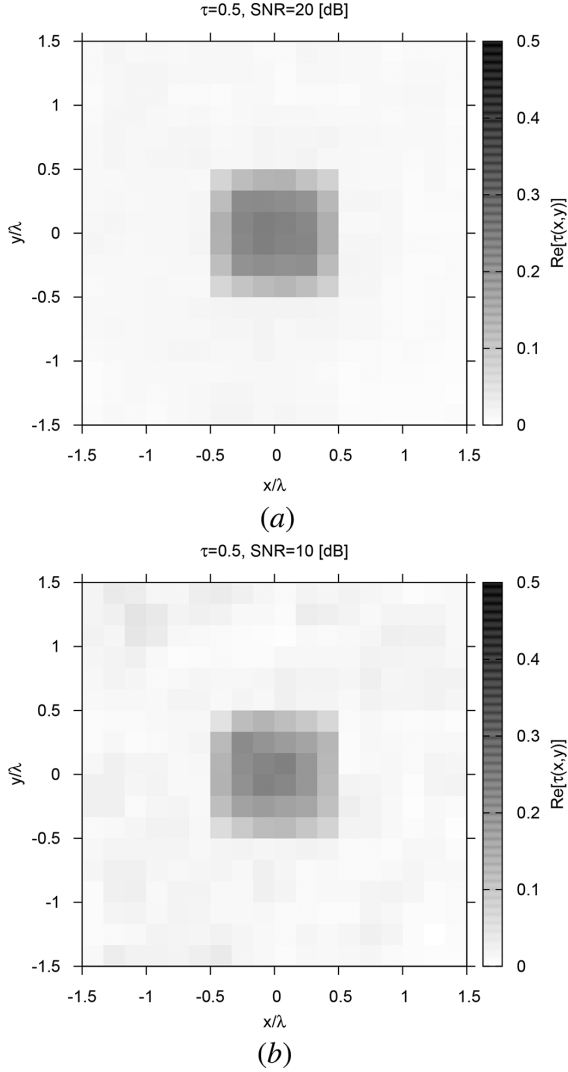


Fig. 4. Performance Assessment (“Square” profile, $L = 2/3\lambda$, $\tau = 0.5$)—Dielectric profile retrieved with the TV-CS method when (a) SNR = 20 dB and (b) SNR = 10 dB.

In the noiseless case [Fig. 1(a)], the plot of the total error index, ξ_{tot} , versus μ ($\mu \in [10^{-10}, 10^{10}]$) shows that ξ_{tot} can vary of more than one order in magnitude depending on the parameter value [$(\xi_{\text{tot}}|_{\mu=2 \times 10^{-2}} / \xi_{\text{tot}}|_{\mu=2}) > 2.5 \times 10^1$ —Fig. 1(a)] and the best reconstruction has been yielded with $\mu \approx 2(\xi_{\text{tot}}|_{\mu=2} \approx 4.7 \times 10^{-4})$. Similar outcomes can be drawn when noisy data are at hand [SNR $\in [5, 20]$ dB—Fig. 1(a)]. Although, as expected, the minimum value of the ξ_{tot} plots increases with the noise level (e.g., $\min_{\mu} \{\xi_{\text{tot}}|_{\text{SNR}=20 \text{ dB}}\} \approx 6.5 \times 10^{-4}$ vs. $\min_{\mu} \{\xi_{\text{tot}}|_{\text{SNR}=5 \text{ dB}}\} \approx 5.5 \times 10^{-3}$), the optimal value of μ still turns out to be

$$\mu^{\text{opt}} = 2.0. \quad (16)$$

Therefore, such a value will be set hereinafter as default.

As for β , the behavior of the total integral error within $\beta \in [10^{-10}, 10^{10}]$ and for noiseless conditions [black line—Fig. 1(b)] suggests that a satisfactory accuracy ($\xi_{\text{tot}} \approx 0.1\%$) can be yielded by choosing the β value in a quite broad

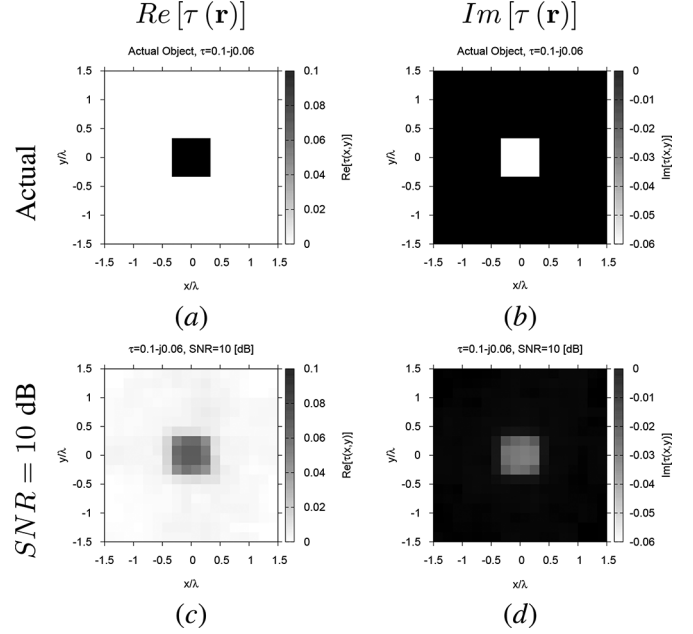


Fig. 5. Performance Assessment (Lossy “Square” profile, $L = 2/3\lambda$, $\tau = 0.1 - j0.06$)—Real (a),(c) and imaginary (b),(d) parts of (a),(b) the actual and (c),(d) the retrieved dielectric profile when SNR = 10 dB.

range ($\xi_{\text{tot}} \leq 1.7 \times 10^{-3}$ when $\beta \in [2.0 \times 10^{-1}, 2.0 \times 10^3]$) even though the minimum error occurs at $\beta \approx 2.0 \times 10^2$ ($\xi_{\text{tot}}|_{\beta \approx 2.0 \times 10^2} \approx 4.7 \times 10^{-4}$). When varying the SNR, setting $\beta \approx 2.0 \times 10^2$ still represents a good trade-off choice, thus such a setup value

$$\beta^{\text{opt}} = 2.0 \times 10^2 \quad (17)$$

will be assumed as reference in the following.

To give the interested reader also a visual feedback about the inversion accuracy when using the optimal parameter setup, Fig. 2 shows the reconstructed profiles in noiseless conditions [Fig. 2(b)— $\xi_{\text{tot}}|_{\text{SNR}=\infty} \approx 4.7 \times 10^{-4}$] and when SNR = 20 dB [Fig. 2(c)], SNR = 10 dB [Fig. 2(d)], and SNR = 5 dB [Fig. 2(e)]. As it can be observed, the location and the size of the scatterer as well as the contrast profile within D can be clearly inferred also in the presence of blurred data [$\xi_{\text{tot}}|_{\text{SNR}=20 \text{ dB}} \approx 6.5 \times 10^{-4}$ —Fig. 2(c); $\xi_{\text{tot}}|_{\text{SNR}=10 \text{ dB}} \approx 2.7 \times 10^{-3}$ —Fig. 2(d); $\xi_{\text{tot}}|_{\text{SNR}=5 \text{ dB}} \approx 5.6 \times 10^{-3}$ —Fig. 2(d)].

B. TV-CS Performance Assessment

To analyze the potentialities of the TV-CS algorithm in detecting non-sparse piecewise-constant scatterers, the same target of Fig. 2(a) has been imaged next by first varying the contrast values within the range of validity of the BA approximation [$\tau \in [0.01, 0.7]$ —Fig. 3(a)]⁶. With reference to the case SNR = 20 dB, larger errors occur when the contrast grows [e.g., $\xi_{\text{tot}}|_{\tau=0.01} \approx 6.1 \times 10^{-5}$ vs. $\xi_{\text{tot}}|_{\tau=0.7} \approx 4.0 \times 10^{-2}$ —Fig. 3(a)] as actually expected in first-order BA-based methodologies because of the increasing inaccuracy of (2) [27]. Nevertheless, ξ_{tot} turns out always below 5% whatever the scatterer contrast [Fig. 3(a)]. Moreover,

⁶Given the scatterer size at hand, $\tau \approx 0.7$ turns out to be the upper limit for the validity of the BA [50].

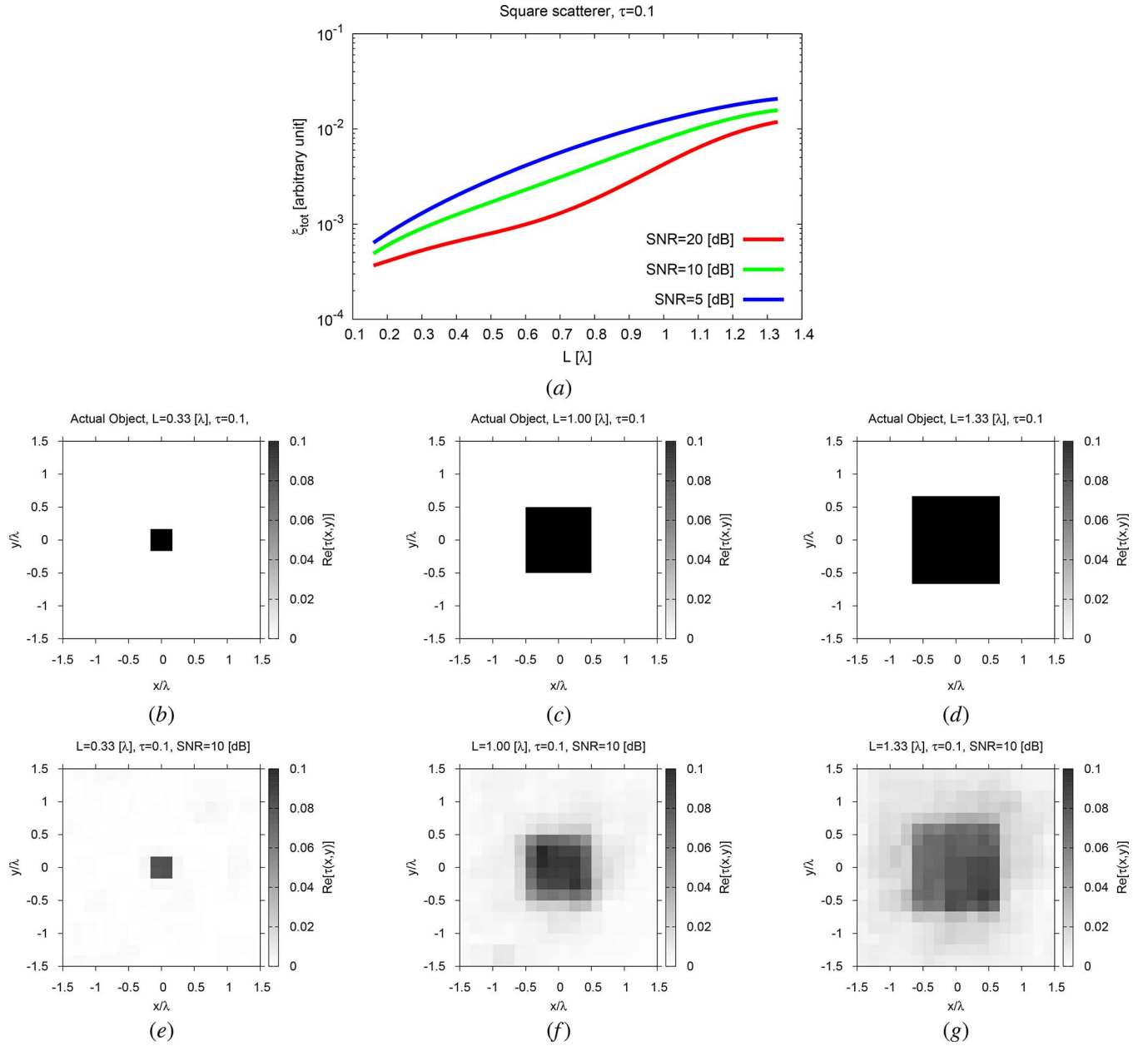


Fig. 6. Performance Assessment (“Square” profile, $\tau = 0.1$)—Behavior of ξ_{tot} versus L for different SNR values (a). Actual (b)–(d) and retrieved (e)–(g) dielectric profiles retrieved with the TV-CS method when SNR = 10 [dB] and (b),(e) $L = \lambda/3$, (c),(f) $L = 1.0\lambda$, and (d),(g) $L = 4/3\lambda$.

only some minor “blurring” effects appear close to the τ upper bound [e.g., $\tau = 0.5$ —Fig. 4(a); $\xi_{\text{tot}}|_{\tau=0.5}^{\text{SNR}=20 \text{ dB}} \approx 2.6 \times 10^{-2}$]. By also analyzing the behaviors of the internal [red line—Fig. 3(b)] and external [red line—Fig. 3(c)] errors, we can observe that, even though the reconstruction accuracy reduces when τ increases both inside [e.g., $\xi_{\text{int}}|_{\tau=0.01} \approx 8.6 \times 10^{-4}$ vs. $\xi_{\text{int}}|_{\tau=0.7} \approx 3.1 \times 10^{-1}$ —Fig. 3(b)] and outside [e.g., $\xi_{\text{ext}}|_{\tau=0.01} \approx 1.9 \times 10^{-5}$ vs. $\xi_{\text{ext}}|_{\tau=0.7} \approx 2.6 \times 10^{-2}$ —Fig. 3(c)] the scatterer support, ξ_{ext} is always significantly smaller than ξ_{int} [e.g., $\xi_{\text{int}}|_{\tau=0.2} \approx 2.7 \times 10^{-2}$ —Fig. 3(b) vs. $\xi_{\text{ext}}|_{\tau=0.2} \approx 2.0 \times 10^{-3}$ —Fig. 3(c)] for a given τ value. This seems to indicate that the TV-CS method is very robust against artifacts lying outside the target support, while the estimation of the scatterer contrast can be slightly inaccurate when larger τ are handled Fig. 4(b)].

Analogous conclusions can be drawn for smaller SNR values [green line—SNR = 10 dB, blue line—SNR = 5 dB; Fig. 3(a)–(c)]. As a matter of fact, ξ_{tot} [Fig. 3(a)], ξ_{int} [Fig. 3(b)], and ξ_{ext} [Fig. 3(c)] behave similarly to the case of SNR = 20 dB. Moreover, it is worth noticing that the total error in reconstructing stronger scatterers is almost independent on the noise level (e.g., $(\xi_{\text{tot}}|_{\tau=0.7}^{\text{SNR}=5 \text{ dB}} / \xi_{\text{tot}}|_{\tau=0.7}^{\text{SNR}=20 \text{ dB}}) \approx 1.2$), while it is significantly affected by the SNR value for low contrasts (e.g., $(\xi_{\text{tot}}|_{\tau=0.05}^{\text{SNR}=5 \text{ dB}} / \xi_{\text{tot}}|_{\tau=0.05}^{\text{SNR}=20 \text{ dB}}) \approx 11.2$). This is also evident in the behavior of ξ_{int} [Fig. 3(b)] and ξ_{ext} [Fig. 3(c)] versus τ and it suggests that the reduced performance for large τ is mainly due to the inaccuracy of the BA, while the noise level has a negligible impact. For completeness, the sample reconstruction when $\tau = 0.5$ and SNR = 10 dB is provided [Fig. 4(b)— $\xi_{\text{tot}} \approx 2.9 \times 10^{-2}$].

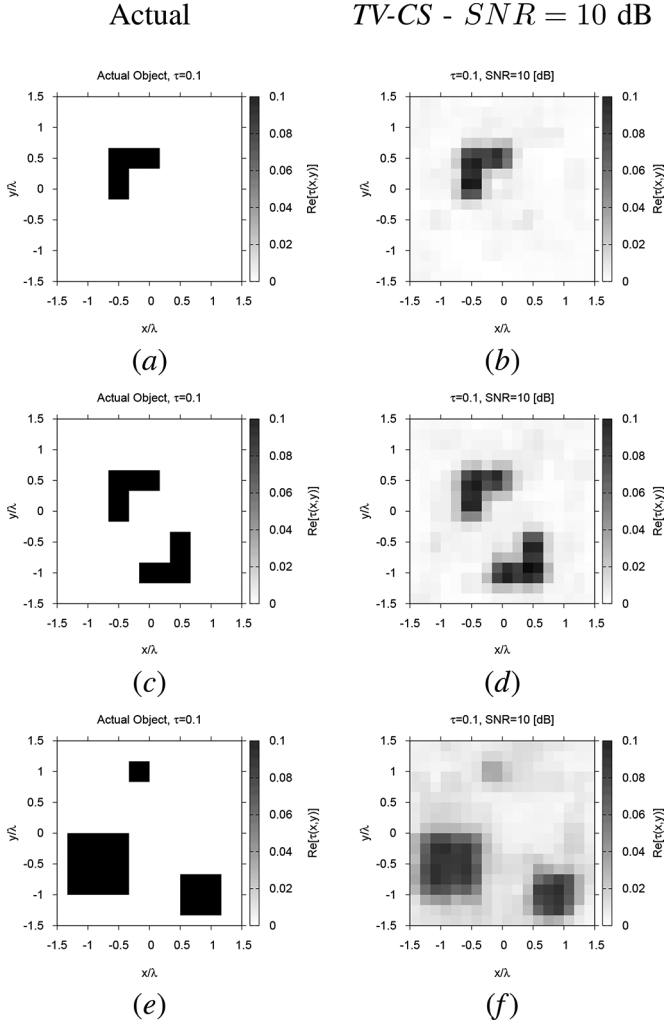


Fig. 7. Performance Assessment ($\tau = 0.1$; SNR = 10 dB)—Actual (a),(c),(e) and retrieved (b),(d),(f) dielectric profiles with the TV-CS method for the (a),(b) “Single- L ,” (c),(d) “Double- L ,” and (e),(f) “Three-squares” scattering configurations.

The effectiveness of the TV-CS method is also confirmed when dealing with lossy dielectric profiles [Fig. 5(a)–(b)]. In fact, the estimated contrast profile for a $L = (2\lambda/3)$ square scatterer with $\tau = 0.1 - j0.06$ when SNR = 10 dB shows that the proposed technique correctly retrieves the real [Fig. 5(c)] and imaginary [Fig. 5(d)] parts of τ , despite the non-negligible noise. Such a result, confirmed by the corresponding total error ($\xi_{\text{tot}} \approx 3.94 \times 10^{-3}$ —Fig. 5) is a consequence of the TV-CS intrinsic capability to handle complex quantities, as anticipated in Section III.

The analysis has then be extended to another set of simulations dealing with a square scatterer of contrast $\tau = 0.1$ and variable size, but always within the range of validity of the BA [50]. As expected from BA theory, the inversion depends on the scatterer size as confirmed by the behavior of ξ_{tot} versus L ($L \in [\lambda/6, (4\lambda/3)]$) when SNR = 20 dB [red line—Fig. 6(a)]. For example, $\xi_{\text{tot}}|_{L=\lambda/6}^{\text{SNR}=20 \text{ dB}} \approx 3.6 \times 10^{-4}$ goes up to $\xi_{\text{tot}}|_{L=4\lambda/3}^{\text{SNR}=20 \text{ dB}} \approx 1.2 \times 10^{-2}$, even though the error always remains under $\xi_{\text{tot}} \approx 2\%$ [Fig. 6(a)]. Such an observation, which holds true also for lower noise

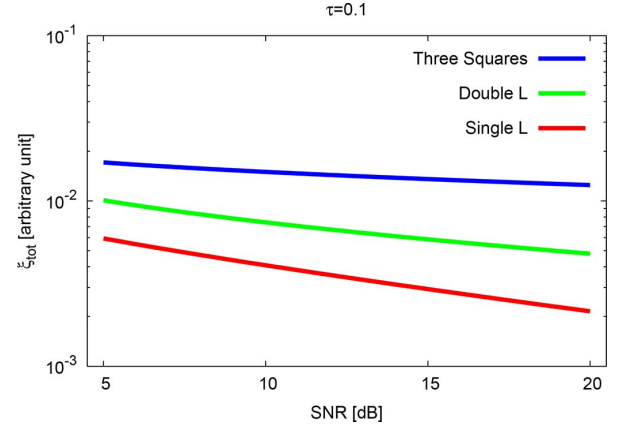


Fig. 8. Performance Assessment ($\tau = 0.1$)—Behavior of ξ_{tot} versus SNR for the “Single- L ,” the “Double- L ,” and the “Three-squares” scattering configurations.

levels [e.g., SNR $\in [5, 10]$ dB—6(a)], is confirmed by the sample images of the reconstructed τ profiles when SNR = 10 dB [$L = \lambda/3$ —Fig. 6(e), $L = \lambda$ —Fig. 6(f), and $L = (4\lambda/3)$ —Fig. 6(g)]. As it can be observed, the retrieval performance reduces as L grows [e.g., Fig. 6(g) vs. Fig. 6(e)]. Notwithstanding, the TV-CS method is always able to image scatterers comprising several connected pixels with an acceptable quality [e.g., $\xi_{\text{tot}}|_{\text{SNR}=10 \text{ dB}} \approx 1.5\%$ when $L = (4\lambda/3)$ that is 64 connected single-resolution pixels—Fig. 6(f)]. This represents a key improvement over similar (i.e., formulated within the same physical framework) state-of-the-art *Compressive Sensing* methodologies that work properly with scatterers comprising few connected pixels or multiple disconnected uniform cells [27].

The successive test case is devoted to evaluate the reliability of the TV-CS method in reconstructing more complex object shapes/contours. The distribution of the estimated contrast profile for the *Single- L* scatterer [Fig. 7(a)] when SNR = 10 dB proves that, despite the harsh conditions, the proposed approach both qualitatively and quantitatively correctly images the target with only some blurring effects [Fig. 7(b)]. Such an outcome is confirmed, also for other SNR values, by the plot of the total reconstruction error versus the noise level in Fig. 8 (red line). Indeed, it turns out that $\xi_{\text{tot}} \leq 5.9 \times 10^{-3}$ whatever the SNR in the range SNR $\in [5, 10]$ dB (Table I).

On the other hand, it is worth pointing out that the applicability of the TV-CS method is not limited to single targets as those considered so far. To support such a claim, the noisy (SNR = 10 dB) reconstructions of the *Double L* [Fig. 7(c)] or the *Three Squares* [Fig. 7(e)] profiles give some indications on the effectiveness of the method [i.e., $\xi_{\text{tot}}|_{\text{Double } L} \approx 6.9 \times 10^{-3}$ —Fig. 7(d); $\xi_{\text{tot}}|_{\text{Double } L} \approx 1.45 \times 10^{-2}$ —Fig. 7(f)] in reconstructing also multiple objects with non-uniform-resolution pixels thanks to the sparsity enforced in the TV sense (7). In accordance with previous analyses, the reconstruction error turns out to be almost independent on the noise level when larger scatterer (closer to the limit of validity of the BA [50]) are at hand ($(\xi_{\text{tot}}|_{\text{SNR}=5 \text{ dB}}/\xi_{\text{tot}}|_{\text{SNR}=20 \text{ dB}}) \approx$

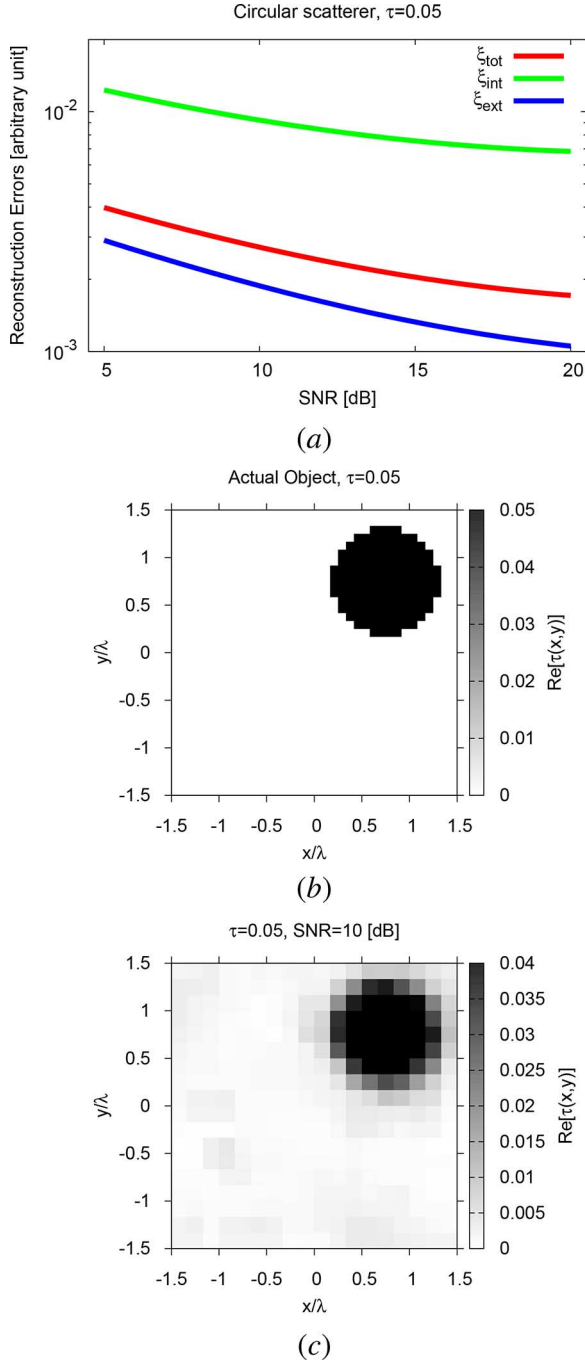


Fig. 9. Performance Assessment (“Circular” profile, $\tau = 0.05$)—Behavior of ξ_{tot} , ξ_{int} , and ξ_{ext} versus SNR (a), and (b) actual and (c) retrieved dielectric profiles when SNR = 10 dB.

1.4 for *Three Squares*—Table I), while it notably depends on the SNR value when retrieving smaller objects ($(\xi_{\text{tot}}|_{\text{SNR}=5 \text{ dB}}/\xi_{\text{tot}}|_{\text{SNR}=20 \text{ dB}}) \approx 2.7$ for *Single L*—Table I). Once again the increasing of ξ_{tot} versus the scatterer size (e.g., red line vs. blue line in Fig. 8) can be mostly attributed to the unavoidable reduction of the accuracy of the BA rather than on the TV-CS inversion solver or the noise level. Such a conclusion is further supported from the analysis of the values of the total reconstruction error in Table I

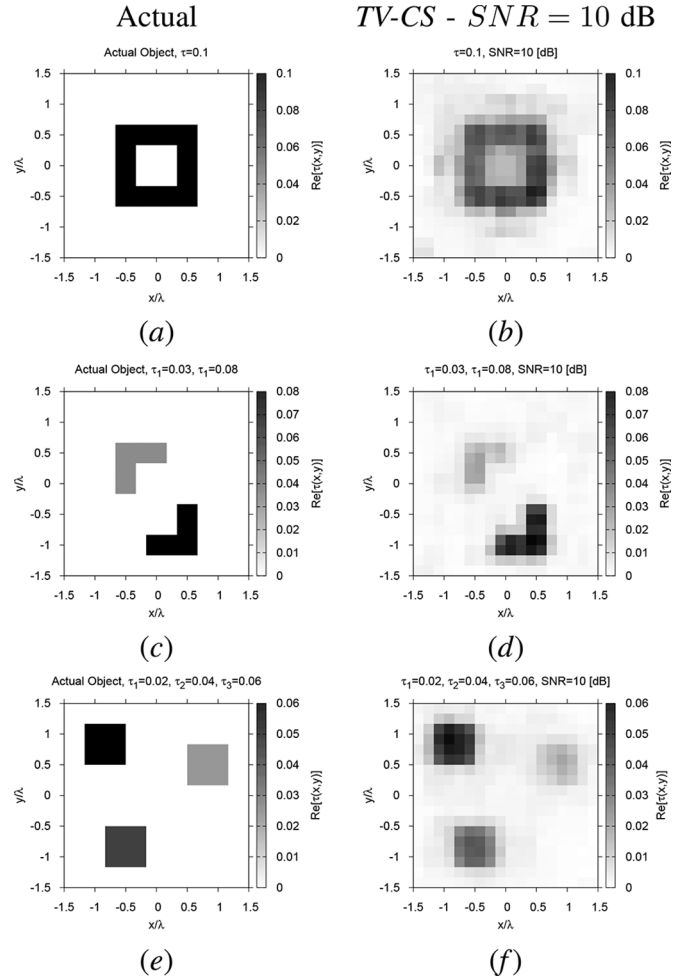


Fig. 10. Performance Assessment (Inhomogeneous profiles, SNR = 10 dB)—Actual (a),(c),(e) and retrieved (b),(d),(f) dielectric profiles with the TV-CS method for the (a),(b) “Hollow-Square,” (c),(d) “Inhomogeneous Double-L,” and (e),(f) “Inhomogeneous Three-squares” scattering configurations.

(e.g., $(\xi_{\text{tot}}|_{\text{SNR}=5 \text{ dB}}/\xi_{\text{tot}}|_{\text{SNR}=20 \text{ dB}}) \approx 1.08$ for *Three Squares*—Table I).

Analogously, it must be remarked that the TV-CS formulation is not constrained to rectangular-based profiles as those considered in Figs. 1–8. The plots of the reconstruction errors versus the noise level [Fig. 9(a)] obtained when imaging a circular scatterer with 0.6λ radius [$\tau = 0.05$ —Fig. 9(b)] confirm the effectiveness of the proposed algorithm [e.g., $\xi_{\text{tot}}|_{\text{SNR}=20 \text{ dB}} \approx 1.71 \times 10^{-3}$ —Fig. 9(a)], despite $\nabla \tau$ has both components with non-zero amplitudes in the Cartesian formulation. Accordingly, it can be concluded that satisfactory reconstructions can be obtained also in low SNR conditions [e.g., Fig. 9(c) vs. Fig. 9(b)], as long as the scatterer contrast is piecewise constant.

Nevertheless, this requirement does not impose the target to be homogeneous. The reconstructions of the *Hollow Square* [Fig. 10(a)], of the *Inhomogeneous Double-L* [Fig. 10(c)], and of the *Inhomogeneous Three Squares* [Fig. 10(e)] profiles show that the TV sparsity constraint (7) also enables to effectively handle single or multiple non-homogeneous scatterers

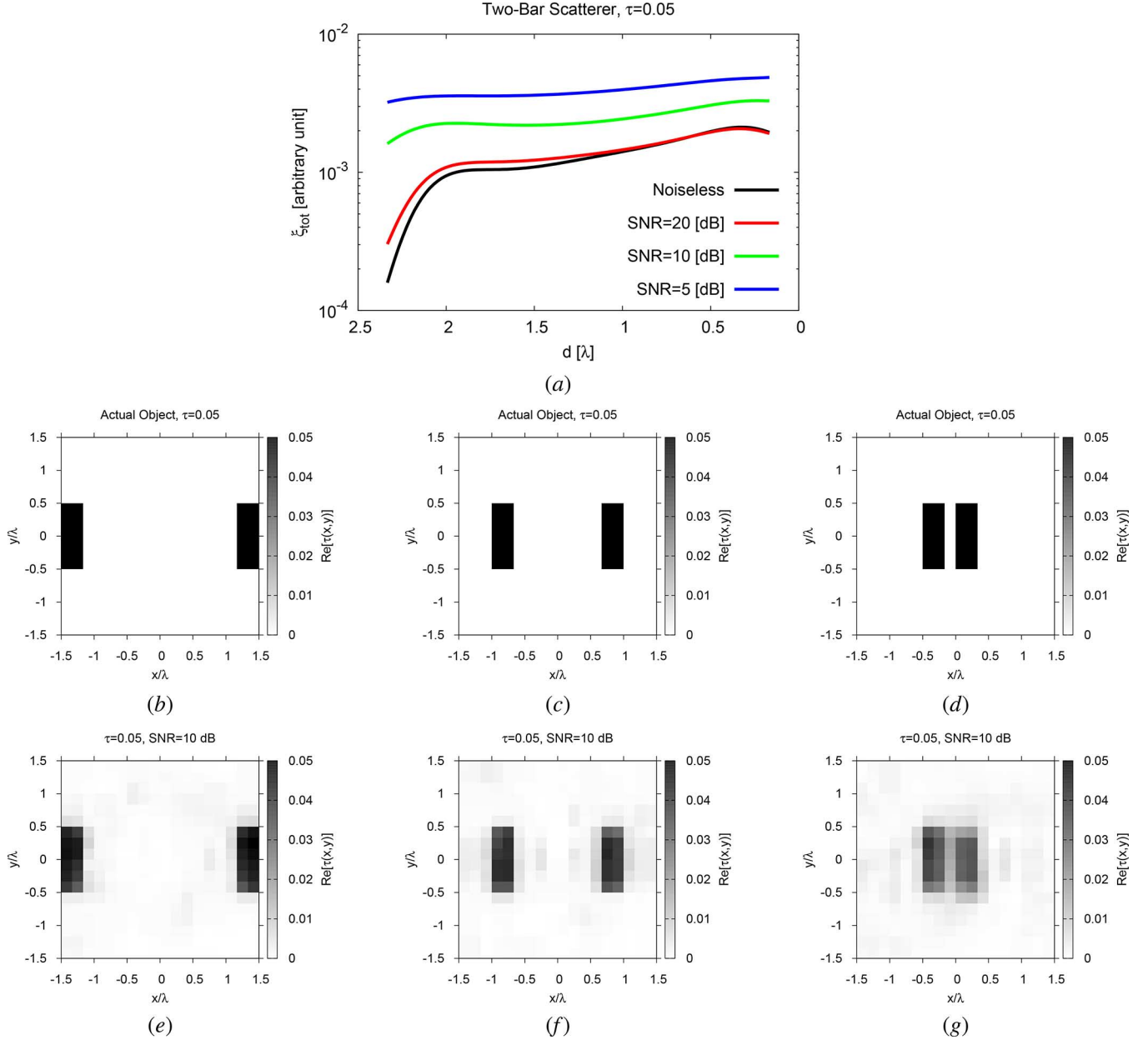


Fig. 11. Performance Assessment (“Two-Bar” profile, $\tau = 0.05$)—Behavior of ξ_{tot} versus L for different SNR values (a). Actual (b)–(d) and retrieved (e)–(g) dielectric profiles retrieved with the TV-CS method when SNR = 10 [dB] and (b),(e) $d = (7\lambda/3)$, (c),(f) $d = (4\lambda/3)$, and (d),(g) $d = \lambda/6$.

with piecewise constant τ [i.e., $\xi_{\text{tot}}|_{\text{Hollow-Square}} \approx 1.25 \times 10^{-3}$ —Fig. 10(b); $\xi_{\text{tot}}|_{\text{Inh. Double } 2L} \approx 3.8 \times 10^{-3}$ —Fig. 10(d); $\xi_{\text{tot}}|_{\text{Inh. Three Squares}} \approx 4.1 \times 10^{-3}$ —Fig. 10(f)]. Moreover, the previous deductions concerning the relationship between the ξ_{tot} increase and the BA accuracy reduction versus the scatterer size are further supported (e.g., $(\xi_{\text{tot}}|_{\text{Inh. Double } 2L} / \xi_{\text{tot}}|_{\text{Inh. Three Squares}}) \approx 0.92$ —Fig. 10).

To investigate the resolution limitations of the approach, a set of experiments has been carried out by assuming the *Two Bar* profile in Fig. 11(b) and varying the inter-bar distance d in the range $d \in [\lambda/6, (7\lambda/3)]$ (Fig. 11). The plots of ξ_{tot} versus d show that although the accuracy diminish with the inter-bar spacing, as expected, the error increment is moderate, especially in low SNR scenario [$(\xi_{\text{tot}}|_{d=(7\lambda/3)}^{\text{SNR}=10 \text{ dB}} / \xi_{\text{tot}}|_{d=(\lambda/6)}^{\text{SNR}=10 \text{ dB}}) \approx 0.49$ —Fig. 11(a)]. This is visually pointed out by the comparable accuracy of the sample

τ profiles when SNR = 10 dB [$d = (7\lambda/3)$ —Fig. 11(e), $d = (4\lambda/3)$ —Fig. 11(f), $d = \lambda/6$ —Fig. 11(g)]. Such result therefore shows that the method enables to distinguish and retrieve piecewise-constant objects whose separation is below $\lambda/2$ [Fig. 11(g)].

The next numerical experiment is aimed at assessing the TV-CS accuracy when using a reduced set of non-adaptive measurements. To this end, the “*Square*” profile [Fig. 2(a)] has been imaged by assuming $M \in [5, 27]$ under various noise conditions [Fig. 12(a)]. The plots of the total reconstruction error versus the number of measurements [Fig. 12(a)] show that the proposed method enables to use much less data than would otherwise be dictated by Nyquist criteria (i.e., $M_{\text{Nyquist}} = 27$ according to the criterion in [54]) without introducing significant distortions [e.g., $(\xi_{\text{tot}}|_{M=15}^{\text{SNR}=20 \text{ dB}} / \xi_{\text{tot}}|_{M=27}^{\text{SNR}=20 \text{ dB}}) \approx 1.087$ —Fig. 12(a)]. This behaviour, observed for all SNR values

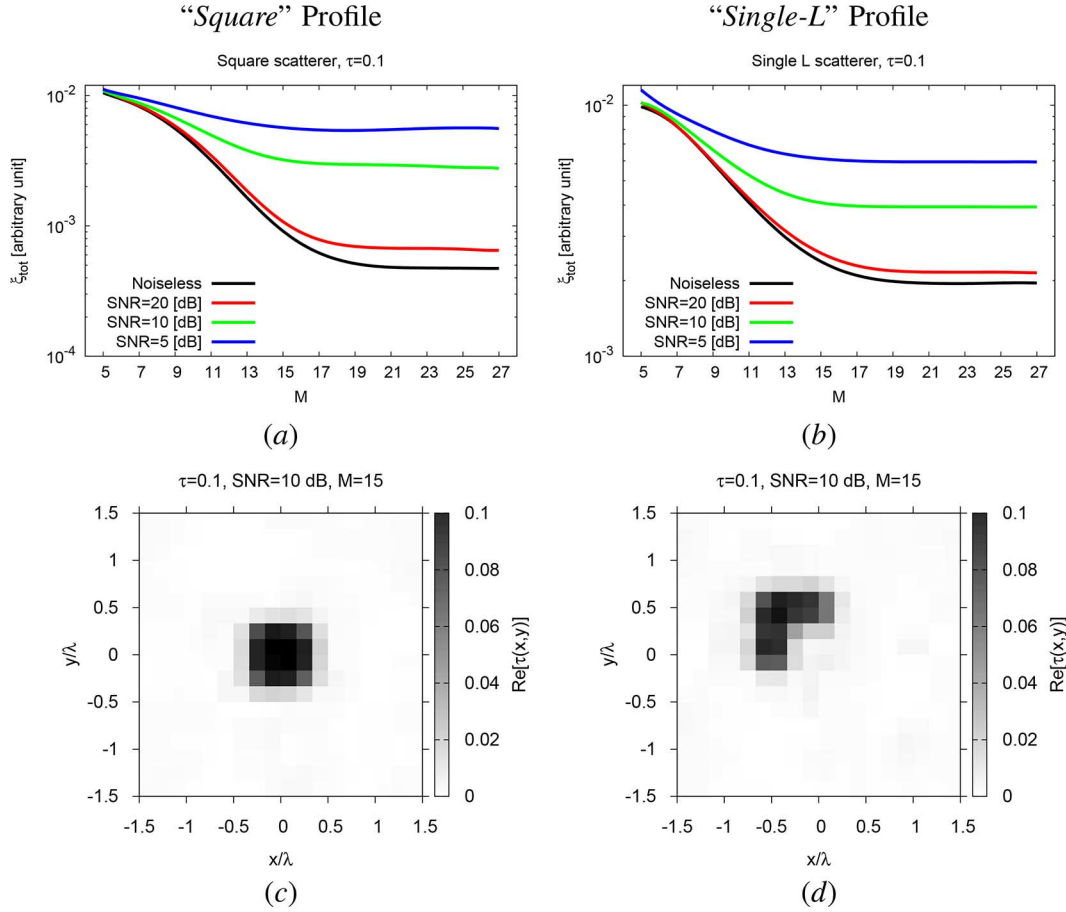


Fig. 12. *Performance Assessment* ($\tau = 0.1$)—Behaviour of ξ_{tot} versus M (a),(b) and dielectric profiles retrieved when $M = 15$, SNR = 10 dB (c),(d) for (a),(c) the “Square” and (b),(d) the “Single-L” scattering configurations.

[e.g., $(\xi_{\text{tot}}|_{\text{SNR}=10 \text{ dB}}^{M=15} / \xi_{\text{tot}}|_{\text{SNR}=10 \text{ dB}}^{M=27}) \approx 1.091$ —Fig. 12(a)], is visually confirmed by the similarity between the retrieved τ profile for $M = 15$ [Fig. 12(c)] and that obtained by processing the complete dataset [Fig. 2(d)] when SNR = 10 dB. On the other hand, the retrieval error significantly increases when $M \leq 14$ [e.g., $(\xi_{\text{tot}}|_{\text{SNR}=20 \text{ dB}}^{M=13} / \xi_{\text{tot}}|_{\text{SNR}=20 \text{ dB}}^{M=27}) \approx 3.061$ —Fig. 12(a)]. This feature is expected from CS theory, as the minimum number of non-adaptive measurements required to correctly retrieve a sparse signal is proportional to its *sparsity* factor [in this case, $|\nabla\tau|_1 = 16$ —Fig. 2(a)] [29].

These conclusions actually do not depend on the scatterer profile. For completeness, Fig. 12(b) resumes the plots of ξ_{tot} versus M for the “L-shaped” profile [Fig. 7(a)], which further remark the TV-CS accuracy also when the number of non-adaptive measurements at hand is significantly below Nyquist threshold [e.g., $(\xi_{\text{tot}}|_{\text{SNR}=10 \text{ dB}}^{M=15} / \xi_{\text{tot}}|_{\text{SNR}=10 \text{ dB}}^{M=27}) \approx 1.098$ —Fig. 12(b)], as also pointed out by the sample reconstruction obtained when $M = 15$, SNR = 10 dB [Fig. 12(d) vs. Fig. 7(b)].

C. Comparative Assessment

For a fair comparison between the proposed deterministic TV-CS method and the available state-of-the-art inversion techniques implemented within the BA, the benchmark target in Fig. 2(a) has been first imaged with a deterministic conjugate-gradient (CG)-based method minimizing

the BA data-misfit function. The image of the τ -distribution retrieved when SNR = 20 dB shows that the CG inversion [Fig. 13(c)] is less accurate than the TV-CS one [Fig. 13(a)]. Such a result is quantitatively confirmed by the corresponding error indexes reported in Fig. 14 ($(\xi_{\text{tot}}|_{\text{CG}}^{\text{SNR}=20 \text{ dB}} / \xi_{\text{tot}}|_{\text{TV-CS}}^{\text{SNR}=20 \text{ dB}}) \approx 112\%$). This behavior becomes even more evident in heavier noisy conditions [e.g., $(\xi_{\text{tot}}|_{\text{CG}}^{\text{SNR}=10 \text{ dB}} / \xi_{\text{tot}}|_{\text{TV-CS}}^{\text{SNR}=10 \text{ dB}}) \approx 200\%$ —Fig. 13(b) vs. Fig. 13(d)]. Moreover, the slope of the curve of $\xi_{\text{tot}}|_{\text{TV-CS}}$ versus SNR results significantly lower than that for the CG (Fig. 14). As expected, the exploitation of the *a-priori* information on the piecewise-constant nature of the scatterers through the TV-CS formulation gives a non-negligible advantage in terms of inversion accuracy and robustness.

Successively, the comparative assessment has been extended by applying the BA Multi-Task Bayesian CS technique (MT-BCS) [27] to the same scattering scenario. The contrast profiles estimated with the MT-BCS when SNR = 20 dB [Fig. 13(e)] and SNR = 10 dB [Fig. 13(f)] turn out significantly poorer [e.g., Fig. 13(e) vs. Fig. 13(a)], as also remarked by the ξ_{tot} plot in Fig. 14, because of the nature of the target whose support occupies 16 connected single-resolution pixels [Fig. 2(a)]. Such a result gives a clear indication on the capability of the TV-CS scheme to overcome the intrinsic theoretical limitations of state-of-the-art CS imaging techniques [27] when dealing with multiple-connected-pixels contrast profiles.

TABLE I
PERFORMANCE ASSESSMENT—ERROR INDEXES

Profile SNR [dB]	“Single L”		“Double L”		“Three Squares”	
	$\tau = 0.1$	$\tau = 0.5$	$\tau = 0.1$	$\tau = 0.5$	$\tau = 0.1$	$\tau = 0.5$
20	2.2×10^{-3}	2.3×10^{-2}	4.8×10^{-3}	4.5×10^{-2}	1.2×10^{-2}	9.2×10^{-2}
10	3.9×10^{-3}	2.7×10^{-2}	7.0×10^{-3}	4.9×10^{-2}	1.5×10^{-2}	9.6×10^{-2}
5	5.9×10^{-3}	3.1×10^{-2}	1.0×10^{-2}	5.7×10^{-2}	1.7×10^{-2}	1.0×10^{-1}

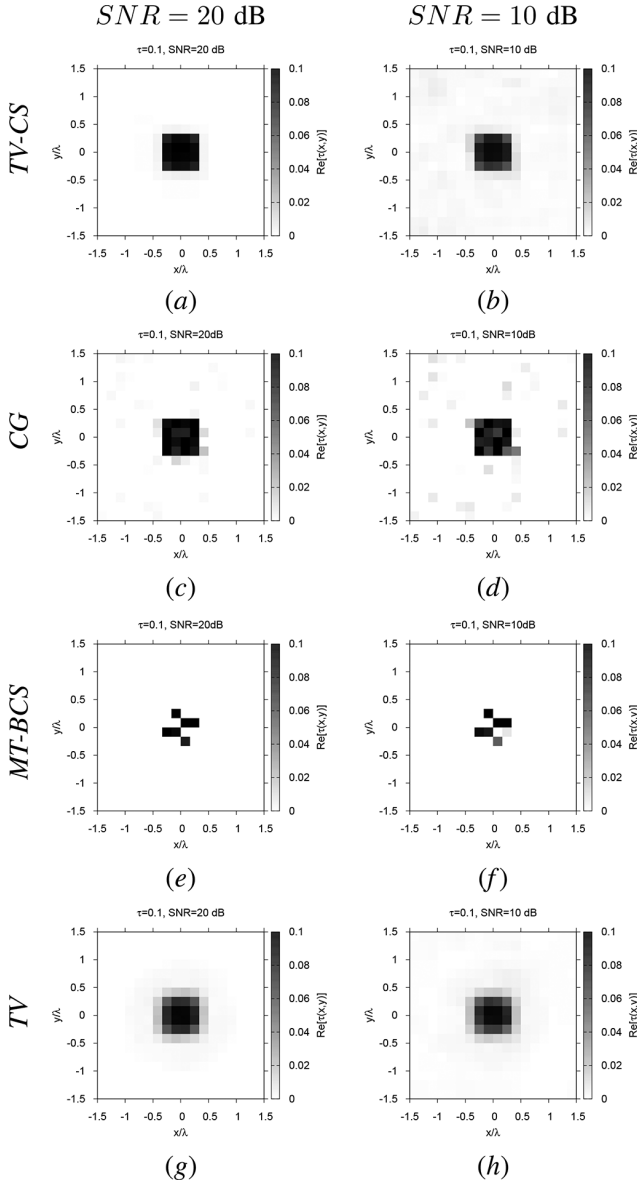


Fig. 13. Comparative Assessment (“Square” profile, $L = 2/3\lambda$, $\tau = 0.1$)—Dielectric profiles retrieved with (a)(b) the TV-CS, (c),(d) the MT-BCS, (e),(f) the CG, and (g),(h) the TV methods when (a),(c),(e),(g) SNR = 20 dB and (b),(d),(f),(h) SNR = 10 dB.

The comparison has been further enlarged by solving the same problem with a state-of-the-art TV methodology [45] which, for the sake of fairness, has been formulated and implemented within the BA. The reported reconstructions indicate that the total-variation method turns out less accurate than the proposed TV-CS both in low noise [Fig. 13(a) vs. Fig. 13(g)] and in noisy conditions [Fig. 13(b) vs. Fig. 13(h)]. More specifically, the TV approach exhibits a “blurring” effect on the

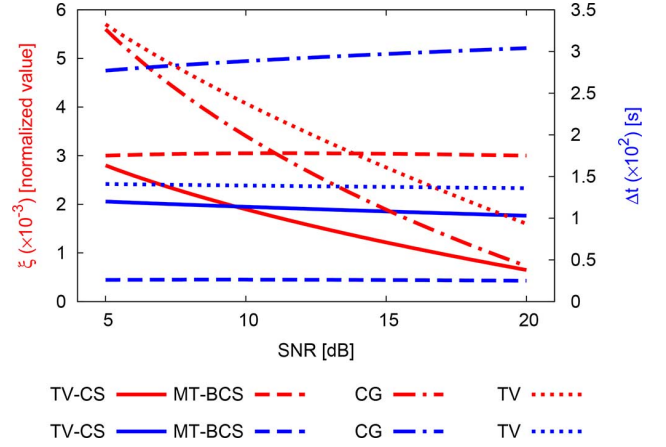


Fig. 14. Comparative Assessment (“Square” profile, $L = 2/3\lambda$, $\tau = 0.1$)—Behavior of ξ_{tot} and Δt versus SNR for the TV-CS, the MT-BCS, the CG, and the TV techniques.

reconstructions [e.g., Fig. 13(b)]. This effect, which causes an increase in the corresponding ξ_{tot} values (Fig. 14), is theoretically expected since state-of-the-art TV aims at minimizing the ℓ_2 norm of $\nabla \tau$ (i.e., its energy) [45], rather than its ℓ_1 norm (see Section III). Consequently, smooth contrast profiles [e.g., Fig. 13(h)] not complying with the piecewise-constant τ at hand [Fig. 2(a)] are obtained.

As for the computational efficiency, the plots of the inversion time (Δt)⁷ (blue lines—Fig. 14) indicate that the CS-based probabilistic approach in [27] is faster than that the deterministic one proposed in this paper ($(\Delta t|_{\text{MT-BCS}}/\Delta t|_{\text{TV-CS}}) \approx 0.25$), but it is quite unreliable when reconstructing “non-sparse” pixel-based scatterers (Fig. 13). On the contrary, the CG- and the TV-based techniques are significantly slower than the TV-CS ($(\Delta t|_{\text{CG}}/\Delta t|_{\text{TV-CS}}) \approx 3.0$, $(\Delta t|_{\text{TV}}/\Delta t|_{\text{TV-CS}}) \approx 1.5$ —Fig. 13).

V. CONCLUSION

An innovative TV-CS inversion method has been proposed to image two-dimensional non-sparse targets with piecewise-constant contrasts that satisfy the BA. A selected set of representative numerical results has been reported to assess the features of the proposed technique in terms of accuracy, flexibility, robustness to noise, and numerical efficiency.

The numerical assessment has shown that:

- satisfactory reconstructions can be yielded in a wide range of working conditions (e.g., different SNRs) by setting the control parameters of TV-CS according to the optimal setup provided in Section IV-A;

⁷For a fair comparison, all the CPU-times refer to non-optimized Matlab codes running on a 3.0 GHz single-core desktop PC.

- unlike existing CS-based imaging methods [Fig. 13(e)–(f)], the proposed approach provides reliable performance for non-sparse scatterers (Fig. 6) even though its accuracy depends on the size and the contrast of the scatterer [Figs. 3 and 6(a)] as a consequence of the underlying BA (Sections IV-B–IV-C);
- thanks to the exploitation of the *a-priori* information through the Total-Variation Compressive Sensing formulation, such a CS-based deterministic method turns out to be a reliable and efficient alternative to other state-of-the-art deterministic tools (including standard TV solvers) (Fig. 14);
- the TV-CS inversion method works properly also when multiple non-sparse scatterers with different shapes/sizes are at hand (Fig. 7), as well as when handling a reduced set of non-adaptive measurements (Fig. 12).

Future works, beyond the scope of the present paper, will be aimed at extending the TV-CS imaging approach to non-approximated inverse scattering problems formulated within the contrast source framework [26] as well as to deal with different illumination setups (e.g., TE or multi-frequency) in order to apply it in the detection of delaminations in composite materials [39], of foam defects [40], and of hidden tunnels [41], [42]. Moreover, the generalization to full 3D scenarios is currently under investigation.

ACKNOWLEDGMENT

The authors wish to thank Dr. Li, Dr. Yin, and Dr. Zhang for sharing the TVAL3 code online [55].

REFERENCES

- [1] J. V. Candy and C. Pichot, "Active microwave imaging: A model-based approach," *IEEE Trans. Antennas Propag.*, vol. 39, no. 3, pp. 285–290, Mar. 1991.
- [2] A. Baussard, E. L. Miller, and D. Lesselier, "Adaptive multiscale reconstruction of buried objects," *Inverse Probl.*, vol. 20, pp. S1–S15, Dec. 2004.
- [3] W. C. Chew and D. Lesselier, "Special issue on electromagnetic characterization of buried obstacles," *Inverse Probl.*, vol. 20, no. 6, Dec. 2004.
- [4] C.-C. Chen, J. T. Johnson, M. Sato, and A. G. Yarovoy, "Special issue on "Subsurface sensing using ground-penetrating radar,"" *IEEE Trans. Geosci. Remote Sens.*, vol. 45, no. 8, Aug. 2007.
- [5] R. Zoughi, *Microwave Nondestructive Testing and Evaluation*. Amsterdam, The Netherlands: Kluwer Academic, 2000.
- [6] S. Kharkovsky and R. Zoughi, "Microwave and millimeter wave non-destructive testing and evaluation—Overview and recent advances," *IEEE Instrum. Meas. Mag.*, vol. 10, pp. 26–38, Apr. 2007.
- [7] C. C. Chiu, C. H. Sun, C. L. Li, and C. H. Huang, "Comparative study of some population-based optimization algorithms on inverse scattering of a two-dimensional perfectly conducting cylinder in slab medium," *IEEE Trans. Geosci. Remote Sens.*, vol. 51, pp. 2302–2315, Apr. 2013.
- [8] M. Moghaddam and W. C. Chew, "Nonlinear two-dimensional velocity profile inversion using time domain data," *IEEE Trans. Geosci. Remote Sens.*, vol. 30, no. 1, pp. 147–156, Jan. 1992.
- [9] S. S. Saatchi and M. Moghaddam, "Estimation of crown and stem water content and biomass of boreal forest using polarimetric SAR imagery," *IEEE Trans. Geosci. Remote Sens.*, vol. 38, no. 2, pp. 697–709, Mar. 2000.
- [10] A. Tabatabaenejad and M. Moghaddam, "Inversion of subsurface properties of layered dielectric structures with random slightly rough interfaces using the method of simulated annealing," *IEEE Trans. Geosci. Remote Sens.*, vol. 47, no. 7, pp. 2035–2046, Jul. 2009.
- [11] A. Franchois and C. Pichot, "Microwave imaging-complex permittivity reconstruction with a Levenberg–Marquardt method," *IEEE Trans. Antennas Propag.*, vol. 45, no. 2, pp. 203–215, Feb. 1997.
- [12] P. M. Meaney, M. W. Fanning, D. Li, S. P. Poplack, and K. D. Paulsen, "A clinical prototype for active microwave imaging of the breast," *IEEE Trans. Microwave Theory Tech.*, vol. 48, pp. 1841–1853, Nov. 2000.
- [13] M. El-Shenawee and E. Miller, "Spherical harmonics microwave algorithm for shape and location reconstruction of breast cancer tumors," *IEEE Trans. Med. Imag.*, vol. 25, pp. 1258–1271, Oct. 2006.
- [14] T. Rubk, P. M. Meaney, P. Meincke, and K. D. Paulsen, "Nonlinear microwave imaging for breast-cancer screening using gauss-newton's method and the CGLS inversion algorithm," *IEEE Trans. Antennas Propag.*, vol. 55, pp. 2320–2331, Aug. 2007.
- [15] Q. Fang, P. Meaney, and K. Paulsen, "Viable three-dimensional medical microwave tomography: Theory and numerical experiments," *IEEE Trans. Antennas Propag.*, vol. 58, pp. 449–458, Feb. 2010.
- [16] S. C. Hagness, E. C. Fear, and A. Massa, "Guest editorial: Special cluster on microwave medical imaging," *IEEE Antennas Wireless Propag. Lett.*, vol. 11, pp. 1592–1597, 2012.
- [17] C. C. Chiu and C. H. Sun, "Through-wall imaging for a metallic cylinder," *Nondestructive Test. Eval.*, vol. 28, pp. 72–81, Jan. 2013.
- [18] P. Lobel, R. E. Kleinman, C. Pichot, L. Blanc-Feraud, and M. Barlaud, "Conjugate-gradient method for solving inverse scattering with experimental data," *IEEE Antennas Propag. Mag.*, vol. 38, no. 3, pp. 48–51, Jun. 1996.
- [19] A. Zakaria and J. LoVetri, "Application of multiplicative regularization to the finite-element contrast source inversion method," *IEEE Trans. Antennas Propag.*, vol. 59, no. 9, pp. 3495–3498, Sep. 2011.
- [20] P. Mojab, J. LoVetri, and L. Shafai, "A multiplicative regularized Gauss-Newton inversion for shape and location reconstruction," *IEEE Trans. Antennas Propag.*, vol. 59, no. 12, pp. 4790–4802, Dec. 2011.
- [21] G. Oliveri, L. Poli, P. Rocca, and A. Massa, "Bayesian compressive optical imaging within the Rytov approximation," *Opt. Lett.*, vol. 37, no. 9, pp. 1760–1762, 2012.
- [22] M. Bertero and P. Boccacci, *Introduction to Inverse Problems in Imaging*. Bristol, U.K.: IOP, 1998.
- [23] P. Mojab and J. LoVetri, "Overview and classification of some regularization techniques for the Gauss-Newton inversion method applied to inverse scattering problems," *IEEE Trans. Antennas Propag.*, vol. 57, no. 9, pp. 2658–2665, Sep. 2009.
- [24] E. A. Marengo, R. D. Hernandez, Y. R. Citron, F. K. Gruber, M. Zambrano, and H. Lev-Ari, "Compressive sensing for inverse scattering," in *Proc. XXIX URSI General Assembly*, Chicago, IL, USA, Aug. 7–16, 2008.
- [25] E. A. Marengo, "Compressive sensing and signal subspace methods for inverse scattering including multiple scattering," presented at the IEEE Geosci. Remote Sensing Symp., Boston, MA, USA, Jul. 7–11, 2008.
- [26] G. Oliveri, P. Rocca, and A. Massa, "A Bayesian compressive sampling-based inversion for imaging sparse scatterers," *IEEE Trans. Geosci. Remote Sens.*, vol. 49, no. 10, pp. 3993–4006, Oct. 2011.
- [27] L. Poli, G. Oliveri, and A. Massa, "Microwave imaging within the first-order Born approximation by means of the contrast-field Bayesian compressive sensing," *IEEE Trans. Antennas Propag.*, vol. 60, no. 6, pp. 2865–2879, Jun. 2012.
- [28] R. G. Baraniuk, "Compressive sampling," *IEEE Signal Process. Mag.*, vol. 24, no. 4, pp. 118–124, Jul. 2007.
- [29] E. J. Candes and M. B. Wakin, "An introduction to compressive sampling," *IEEE Signal Process. Mag.*, vol. 25, no. 2, pp. 21–30, Mar. 2008.
- [30] A. Fannjiang, P. Yan, and T. Strohmer, "Compressed remote sensing of sparse object," arXiv, 0904.3994v2, pp. 1–22, 2009.
- [31] S. Ji, Y. Xue, and L. Carin, "Bayesian compressive sensing," *IEEE Trans. Signal Process.*, vol. 56, no. 6, pp. 2346–2356, Jun. 2008.
- [32] L. Poli, G. Oliveri, P. Rocca, and A. Massa, "Bayesian compressive sensing approaches for the reconstruction of two-dimensional sparse scatterers under TE illumination," *IEEE Trans. Geosci. Remote Sensing*, vol. 51, no. 5, pp. 2920–2936, May 2013.
- [33] L. Poli, G. Oliveri, F. Viani, and A. Massa, "MT-BCS-based microwave imaging approach through minimum-norm current expansion," *IEEE Trans. Antennas Propag.*, vol. 61, no. 9, pp. 4722–4732, Sep. 2013.
- [34] F. Viani, L. Poli, G. Oliveri, F. Robol, and A. Massa, "Sparse scatterers imaging through approximated multitask compressive sensing strategies," *Microwave Opt. Technol. Lett.*, vol. 55, no. 7, pp. 1553–1558, July 2013.

- [35] L. Poli, G. Oliveri, and A. Massa, "Imaging sparse metallic cylinders through a local shape function Bayesian Compressive Sensing approach," *J. Opt. Soc. Am. A*, vol. 30, no. 6, pp. 1261–1272, 2013.
- [36] C. Li, "An Efficient Algorithm for Total Variation Regularization With Applications to the Single Pixel Camera and Compressive Sensing," Master's thesis, Rice Univ., Houston, TX, USA, Sep. 2009.
- [37] C. Li, "Compressive Sensing for 3D Data Processing Tasks: Applications, Models, and Algorithms," Ph.D. dissertation, Rice Univ., Houston, TX, USA, Apr. 2011.
- [38] C. Li, H. Jiang, P. Wilford, Y. Zhang, and M. Scheutzw, "A new compressive video sensing framework for mobile broadcast," *IEEE Trans. Broadcast.*, vol. 59, no. 1, pp. 197–205, Mar. 2013.
- [39] R. Zoughi and S. Bakhtiari, "Microwave nondestructive detection and evaluation of disbonding and delamination in layered-dielectric slabs," *IEEE Trans. Instrum. Meas.*, vol. 39, no. 6, pp. 1059–1063, Dec. 1990.
- [40] S. Kharkovsky, J. T. Case, M. A. Abou-Khousa, R. Zoughi, and F. L. Hepburn, "Millimeter-wave detection of localized anomalies in the space shuttle external fuel tank insulating foam," *IEEE Trans. Instrum. Meas.*, vol. 55, no. 4, pp. 1250–1257, Aug. 2006.
- [41] P. Xie, S. L. Grant, N. H. Putnam, N. L. Anderson, and A. Nasseri-Moghaddam, "An improved post-processing technique for array-based detection of underground tunnels," *IEEE J. Sel. Topics Appl. Earth Observ.*, vol. 7, no. 3, pp. 828–837, Mar. 2014.
- [42] L. L. Monte, D. Erricolo, F. Soldovieri, and M. C. Wicks, "Radio frequency tomography for tunnel detection," *IEEE Trans. Geosci. Remote Sens.*, vol. 48, no. 3, pp. 1128–1137, Mar. 2010.
- [43] L. I. Rudin, S. Osher, and E. Fatemi, "Nonlinear total variation based noise removal algorithms," *Phys. D: Nonlinear Phenomena*, vol. 60, no. 1, pp. 259–268, 1992.
- [44] M. Cetin and W. C. Karl, "Feature-enhanced synthetic aperture radar image formation based on nonquadratic regularization," *IEEE Trans. Image Process.*, vol. 10, no. 4, pp. 623–631, Apr. 2001.
- [45] A. Abubakar and P. M. Van den Berg, "Total variation as a multiplicative constraint for solving inverse problems," *IEEE Trans. Image Process.*, vol. 10, no. 9, pp. 1384–1392, Sep. 2001.
- [46] D. Goldfarb and W. Yin, "Second-order cone programming methods for total variation based image restoration," *SIAM J. Scient. Comput.*, vol. 27, no. 2, pp. 622–645, 2005.
- [47] E. J. Candes and T. Tao, "Decoding by linear programming," *IEEE Trans. Inf. Theory*, vol. 51, no. 12, pp. 4203–4215, Dec. 2005.
- [48] J. Bioucas-Dias and M. Figueiredo, "A new TwIST: Two-step iterative thresholding algorithm for image restoration," *IEEE Trans. Imag. Process.*, vol. 16, no. 12, pp. 2992–3004, Dec. 2007.
- [49] S. Becker, J. Robin, and E. Candes, NESTA: A Fast and Accurate First-Order Method for Sparse Recovery California Inst. Techn., Tech. Rep., Apr. 2009.
- [50] M. Slaney, A. C. Kak, and L. E. Larsen, "Limitations of imaging with first-order diffraction tomography," *IEEE Trans. Microw. Theory Tech.*, vol. 32, no. 8, pp. 860–874, Aug. 1984.
- [51] S. Nash and A. Sofer, *Linear and Non-Linear Programming*. Burr Ridge, USA: McGraw-Hill Higher Education, 1996.
- [52] D. W. Peacema and H. H. Rachford, "The numerical solution of parabolic and elliptic differential equations," *J. Soc. Ind. Appl. Math.*, vol. 3, pp. 28–41, 1955.
- [53] J. H. Richmond, "Scattering by a dielectric cylinder of arbitrary cross shape," *IEEE Trans. Antennas Propag.*, vol. 13, no. 3, pp. 334–341, May 1965.
- [54] O. M. Bucci and G. Franceschetti, "On the degrees of freedom of scattered fields," *IEEE Trans. Antennas Propag.*, vol. 37, no. 7, pp. 918–926, Jul. 1989.
- [55] C. Li, W. Yin, and Y. Zhang, "TVAL3 code," 2011 [Online]. Available: www.caam.rice.edu/~optimization/L1/TVAL3/



Giacomo Oliveri (M'07–SM'13) received the B.S. and M.S. degrees in telecommunications engineering and the Ph.D. degree in space sciences and engineering from the University of Genoa, Italy, in 2003, 2005, and 2009 respectively.

He is currently an Assistant Professor at the Department of Information Engineering and Computer Science, University of Trento, and a member of the ELEDIA Research Center. He has been a Visiting Researcher at the Laboratoire des signaux et systèmes (L2S)@Supélec, Paris, France, in 2012 and 2013. In

2014, he was an Invited Associate Professor at the University of Paris Sud, Paris, France. He is author/coauthor of over 200 peer reviewed papers on international journals and conferences. His research work is mainly focused on electromagnetic direct and inverse problems, system-by-design and metamaterials, and antenna array synthesis.

Dr. Oliveri serves as an Associate Editor of the *International Journal of Distributed Sensor Networks* and of the *Microwave Processing Journal*.



Nicola Anselmi (S'13) received the B.S. degree from the University of Padova, Italy, in 2009 and the M.S. degree from the University of Trento, Italy, in 2012, both in telecommunication engineering. Currently, he is working toward the Ph.D. degree at the ICT International Doctoral School of Trento.

Since 2012, he has been a member of the ELEDIA Research Center, University of Trento. His research interests are mainly focused on antenna array design and synthesis and electromagnetic inverse scattering techniques.



Andrea Massa (M'03) received the "Laurea" degree in electronic engineering and the Ph.D. degree in electronics and computer science from the University of Genoa, Genoa, Italy, in 1992 and 1996, respectively.

From 1997 to 1999, he was an Assistant Professor of electromagnetic fields at the Department of Biophysical and Electronic Engineering, University of Genoa. From 2001 to 2004, he was an Associate Professor at the University of Trento, where, since 2005, he has been a Full Professor of electromagnetic fields teaching electromagnetic fields, inverse scattering techniques, antennas and wireless communications, and optimization techniques. At present, he is also the Director of the ELEDIA Research Center, University of Trento. Moreover, he is an Adjunct Professor at Penn State University (USA), and a Visiting Professor at the Missouri University of Science and Technology, USA, Nagasaki University, Japan, the University of Paris Sud, France, and Kumamoto University, Kumamoto, Japan. His research activities are mainly concerned with direct and inverse scattering problems, propagation in complex and random media, analysis/synthesis of antenna systems and large arrays, design/applications of WSNs, cross-layer optimization and planning of wireless/Rf systems, semantic wireless technologies, material-by-design (metamaterials and reconfigurable-materials), and theory/applications of optimization techniques to engineering problems (telecommunications, medicine, and biology). He has published more than 500 scientific publications among which about 250 are in international journals and more than 270 in international conferences where he presented more than 50 invited contributions. He has organized 45 scientific sessions in international conferences and has participated to several technological projects in the European framework (20 EU Projects) as well as at the national and local level with national agencies (75 Projects/Grants).

Prof. Massa is a permanent member of the PIERS Technical Committee, the EuMW Technical Committee, and is an ESoA member, a member of the Inter-University Research Center for Interactions Between Electromagnetic Fields and Biological Systems (ICeMB), and has served as the Italian representative in the General Assembly of the European Microwave Association (EuMA). He has been appointed to the Scientific Board of the "Società Italiana di Elettromagnetismo (SIEM)" and elected to the Scientific Board of the Interuniversity National Center for Telecommunications (CNIT). Recently, he was appointed by the National Agency for the Evaluation of the University System and National Research (ANVUR) as a member of the Recognized Expert Evaluation Group (Area 09, Industrial and Information Engineering) for the evaluation of the researches at the Italian University and Research Center. In addition, he has been appointed as the Italian Member of the Management Committee of the COST Action TU1208 "Civil Engineering Applications of Ground Penetrating Radar." He also serves as an Associate Editor of the IEEE TRANSACTIONS ON ANTENNAS AND PROPAGATION and the "International Journal of Microwave and Wireless Technologies." He is a member of the Editorial Board of the *Journal of Electromagnetic Waves and Applications*.